# A study of transverse momentum distributions of jets produced in $p$-$p$, $p$-$\bar{p}$, $d$-Au, Au-Au, and Pb-Pb collisions at high energies

Hua-Rong Wei, Fu-Hu Liu[1]
*Institute of Theoretical Physics, Shanxi University, Taiyuan, Shanxi 030006, China*

arXiv:1509.08579v1 [nucl-ex] 29 Sep 2015

**Abstract:** The transverse momentum distributions of jets produced in $p$-$p$, $p$-$\bar{p}$, $d$-Au, Au-Au, and Pb-Pb collisions at high energies with different selected conditions are analyzed by using a multi-source thermal model. The multi-component (mostly two-component) Erlang distribution used in our description is in good agreement with the experimental data measured by the STAR, D0, CDF II, ALICE, ATLAS, and CMS Collaborations. Related parameters are extracted from the transverse momentum distributions and some information on different interacting systems are obtained. In the two-component Erlang distribution, the first component has usually two or more sources which are contributed by strong scattering interactions between two quarks or more quarks and gluons, while the second component has mostly two sources which are contributed by harder head-on scattering between two quarks.

**Keywords:** High-energy jets, Transverse momentum distribution, Erlang distribution, Hard scattering, Effective temperature

PACS Nos.: 25.75.Ag, 24.10.Pa, 25.75.Dw

## 1 Introduction

As a new state of matter, quark-gluon plasma (QGP) [1] is different from common plasmas. Generally, the QGP can not be observed directly because its creation needs an extremely high temperature and density. In order to study the properties of the QGP and the mechanisms of parton interactions, a lot of experiments of high energy heavy ion collisions have been performed. Particularly, a high density and high temperature location is formed at the Relativistic Heavy Ion Collider (RHIC) and the Large Hadron Collider (LHC) to create the QGP and to produce multiple final-state particles. By investigating and analyzing these particles, one can obtain some information on the QGP. Hadron jets are one type of final-state particles. People study jets production process to learn the properties of the QGP and the mechanisms of parton interactions both in theories and in experiments [2–4].

The transverse momenta of particles carry important information about the dynamics of particle productions and the evolution process of interacting system formed in nucleus-

[1]E-mail: fuhuliu@163.com; fuhuliu@sxu.edu.cn

nucleus collisions [5]. The transverse momentum ($p_T$) distributions of final-state particles reflect the state of the interacting system at the kinetic stage of freeze-out, when hadrons are no longer interaction and their momenta do not change [6]. Comparing to the low-$p_T$ hadrons which are originated from strong interactions among gluons and sea quarks, high-$p_T$ hadrons are produced due to harder head-on scattering between valent quarks. To analyze high-$p_T$ spectra of final-state particles is then important in studying the mechanisms of high-energy collisions. In addition, the mean transverse momentum of particles, served as a probe for the equation of state of the hadronic matter [7], can partly reflect the effective temperature of interacting system and the transverse excitation degree of emission source in high energy collisions [8].

Due to the hard-scattering of incident partons, partonic jets (including quark and gluon jets) materialize very early during the collisions, which result in plenty of outgoing high-$p_T$ partons. Soon afterwards, a parton fragments into a leading hadron, and a large number of which gather into a cone of hadronic jets which are detected by various detectors such as STAR, D0, CDF II, ALICE, ATLAS, and CMS [9–36]. We are interested in analyzing the transverse momentum distributions of various jets because they can reflect some information of early collisions of partons.

In this paper, we use the multi-component (mostly two-component) Erlang distribution to describe the transverse momentum distributions of jets produced in $p$-$p$, $p$-$\bar{p}$, $d$-Au, Au-Au, and Pb-Pb collisions at high energies, with the framework of a multi-source thermal model [37–39]. The quoted data are at five energies: 0.2, 1.96, 2.76, 7, and 8 TeV per nucleon pair [9–36], and were selected in different detection channels according to different conditions of cone radius, integrated luminosity, pseudorapidity (rapidity) range, and centrality interval. The calculations are performed by using the Monte Carlo method.

## 2 The model and formulism

According to the multi-source thermal model [37–39], we assume that many emission sources are formed in high energy collisions. These emission sources can be separated into a few groups due to different interacting mechanisms in the collisions and different event samples in experimental measurements. Each emission source in the same group has the same transverse excitation degree, and the group is assumed to stay at a local equilibrium state. The total result of a multi-group emission process contributes to the final distribution.

The transverse momentum distribution generated in thermodynamic system obeys an exponential distribution, which is the contribution of one emission source. We have

$$f_{ij}(p_{tij}) = \frac{1}{\langle p_{tij}\rangle} \exp\Big[-\frac{p_{tij}}{\langle p_{tij}\rangle}\Big], \tag{1}$$

where $p_{tij}$ is the transverse momentum contributed by the $i$-th source in the $j$-th group, and $\langle p_{tij}\rangle$ is the mean value of different $p_{tij}$. The folding result of $m_j$ sources in a given (the $j$-th) group is an Erlang distribution, i.e.

$$f_j(p_T) = \frac{p_T^{m_j-1}}{(m_j-1)!\langle p_{tij}\rangle^{m_j}} \exp\Big[-\frac{p_T}{\langle p_{tij}\rangle}\Big], \tag{2}$$

where $p_T$ is the transverse momentum contributed by the $m_j$ sources. If the number of groups is $l$, the total contribution is the multi-component Erlang distribution expressed as

$$f(p_T) = \sum_{j=1}^{l} k_j f_j(p_T), \tag{3}$$

where $k_j$ is the weight contributed by the $j$-th group, which obeys the normalization $\sum k_j = 1$. To describe transverse excitation degree of emission source in the present work, we define a new effective temperature parameter

$$T \equiv \sum_{j=1}^{l} k_j \langle p_{tij} \rangle, \tag{4}$$

which uses the inverse slope parameter $\langle p_{tij} \rangle$.

We shall see from the following section that $p_T$ distributions of jets analyzed in the present work can be mostly fitted by the two-component Erlang distribution. Generally, the first component corresponds to strong scattering interactions where two quarks or more quarks and gluons take part in the process, and the second one corresponds to harder head-on scattering where two quarks take part in the process. All the calculations on $p_T$ distributions are performed by using the Monte Carlo method. For the first component, we have

$$p_T = -\langle p_{ti1} \rangle \sum_{i=1}^{m_1} \ln R_i, \tag{5}$$

and for the second component, we have

$$p_T = -\langle p_{ti2} \rangle \sum_{i=1}^{m_2} \ln R_i, \tag{6}$$

where $R_i$ denote random numbers in $[0, 1]$. The statistics based on weights $k_1$ and $k_2$ $(= 1 - k_1)$ will give $p_T$ distributions. In the case of using the three- or multi-component Erlang distribution, the calculation process of the Monte Carlo method is similar.

We would like to point out that the new effective temperature parameter defined in Eq. (4) is not the real temperature of jets production source, but the mean transverse momentum extracted from the model or experimental data. The real temperature of jets production source should be a reflection of purely thermal motion in the source. The effect of flow or blast wave should be excluded in the extraction of source temperature. Generally, the effective temperature parameter is extracted from the transverse momentum distribution. It includes thermal motion and flow effect, and should be greater than the source temperature. As the mean transverse momentum, the new effective temperature parameter is independent of models.

# 3 Comparison with experimental data

Figure 1 presents $p_T$ distributions of high tower (HT) trigger jets in $p$-$p$ collision (a), HT trigger jets in 0–20% central Au-Au collisions (b), jets from $d$-Au collisions (c), and uncorrected jets in $p$-$p$ collision (d) at center-of-mass energy $\sqrt{s_{NN}} = 0.2$ TeV, where

for $p$-$p$ collision $\sqrt{s_{NN}}$ can be simplified as $\sqrt{s}$. The symbols represent the experimental data of the STAR Collaboration [9–11]. In Figs. 1(a) and 1(b), jet events were selected by an online HT trigger using the anti-$k_T$ algorithm [12] with a cone radius $R = 0.4$, pseudorapidity range $|\eta| < 0.6$, and $p_T > 2.0$ GeV/$c$. The displayed uncertainty of the data is only systematic uncertainty. The data from Fig. 1(c) were recorded during RHIC run 8 (2007–2008) with $R = 0.4$ and $|\eta| < 0.55$. The error bars represent systematic uncertainty and statistical uncertainty. Raw jets in Fig. 1(d) were obtained under the condition of $R = 0.7$, $-0.7 < \eta < 0.9$, and jets $p_T > 5.0$ GeV/$c$. In the figure, some error bars are not visible due to their small values. In this case we regard the marker size as the errors in the calculation. The curves are our results calculated with the two-component Erlang distribution in the framework of the multi-source thermal model by using the Monte Carlo method. The values of free parameters, defined effective temperature parameter $T$, and $\chi^2$ per degree of freedom ($\chi^2$/dof) or $\chi^2$ are shown in Table 1, where $\chi^2$ is used in the case of the number of data points being less than 6 which is the number of free parameters and normalization constant. One can see that the multi-source thermal model describes the experimental data of the considered jets in $p$-$p$, $d$-Au, and Au-Au collisions at $\sqrt{s_{NN}} = 0.2$ TeV. The transverse momentum distributions of mentioned jets are shown to obey the two-component Erlang distribution. For Figs. 1(a), 1(b), and 1(c), all the source numbers of the second groups are 2 and the values of mean excitation degree (defined effective temperature parameter) $T$ extracted from the spectra are close to each other. For the raw jets in Fig. 1(d), the background interference leads to the number of emission sources to increase and the mean excitation degree to decrease.

Figure 2 shows $p_T$ spectra of the leading jets (a)–(c) and all jets (d) that satisfy the event selection described below, produced in $p$-$\bar{p}$ collision at $\sqrt{s} = 1.96$ TeV. The symbols in (a) and (b) represent the experimental data collected by the D0 Collaboration in Run II with an integrated luminosity of 9.7 fb$^{-1}$ [13], while (c) for 3.7 fb$^{-1}$ [14], and (d) the CDF II Collaboration with a cone size of $R = 0.7$, $0.1 < |\eta| < 0.7$, as well as an integrated luminosity of 6 fb$^{-1}$ [15]. The data come from the $Z$ bosons decaying to pairs of leptons $ee$ (a) or $\mu\mu$ (b). The jets in Fig. 2(c) are required to satisfy $p_T > 20$ GeV/$c$ and rapidity $|y| < 3.2$ with a cone radius $R = 0.5$. The error bars in (a) and (b) represent the sum of statistical and systematic uncertainties, and those in (c) and (d) represent statistical and systematic uncertainties respectively. In the figure, for the points with invisible error bars, we measure the marker size as the errors used in the calculation. The curves are our results calculated with the two-component Erlang distribution. The values of free parameters, defined $T$, and $\chi^2$/dof in the calculation are given in Table 1. One can see that the two-component Erlang distribution describes well the experimental data of the jets produced in $p$-$\bar{p}$ collision at $\sqrt{s} = 1.96$ TeV. For the four cases, all the source numbers of the second groups are 2, and the values of $T$ extracted from the spectra are approximately the same.

In Figure 3, we give charged jet $p_T$ spectra produced in Pb-Pb collisions at $\sqrt{s_{NN}} = 2.76$ TeV in different centrality intervals of 0–10% (a), 10–30% (b), 30–50% (c), and 50–80% (d). The experimental data represented by the symbols were measured with a cone radius $R = 0.2$, $|\eta| < 0.5$, anti-$k_T$ jet algorithm [12], charged track $p_T > 0.15$ GeV/$c$, and leading charged track $p_T > 10$ GeV/$c$ by the ALICE Collaboration [16]. The error bars include the total uncertainty. The curves are our fitted results with the two-component

Erlang distribution. The values of free parameters, defined $T$, and $\chi^2$/dof in the calculation are displayed in Table 1. Once more, the two-component Erlang distribution describes well the experimental data of the charged jets produced in Pb-Pb collisions at $\sqrt{s_{NN}} = 2.76$ TeV with different centrality intervals. The fitted source numbers of the second groups are also 2, and the effective temperature parameter $T$ extracted from the spectra slightly increases with increase of the centrality percentage $C$, or $T$ has no obvious change with increase of $C$ in the error range. The figure display of the dependence of $T$ on $C$ will be discussed in the last part of this section.

Figure 4 displays jet $p_T$ spectra produced in $p$-$p$ collision at $\sqrt{s} = 7$ TeV for different conditions. The symbols in (a) and (b) represent the experimental data recorded by the CMS Collaboration [17], and those in (c) and (d) represent the ATLAS Collaboration [18–19]. The first [the black squares in Fig. 4(a)] and the second leading jets [the red circles in Fig. 4(a)], as well as the lepton+jets channel jets with $p_T > 35$ GeV/$c$ [the black squares in Fig. 4(b)] and the dilepton channel jets with $p_T > 30$ GeV/$c$ [the red circles in Fig. 4(b)], were selected corresponding to a total integrated luminosity of 5.0 fb$^{-1}$. In Fig. 4(c), the selected data for the Cambridge-Aachen algorithm jet events where the number of reconstructed primary vertices ($N_{PV}$) composed of at least five tracks is exactly one corresponds to an integrated luminosity of 2 pb$^{-1}$, $R = 1.2$, and $|y| < 2$. The jets shown by the red circles in Fig. 4(c) were split and filtered from those jets with $p_T > 200$ GeV/$c$ represented by the black squares in the same panel. The data for $b$-quark jets ($b$-jets) displayed in Fig. 4(d) were collected with an integrated luminosity of 1.8 fb$^{-1}$ for the single-lepton channels by the black squares and for the dilepton channels by the red circles. The error bars on the data points indicate the statistical uncertainty in Figs. 4(a)–4(c) and systematic uncertainty in Fig. 4(d). For some data points in which the error bars are invisible in the figure, we use the marker size instead of the real error values in our calculation. The curves are our fitted results by the two-component Erlang distribution. The relevant parameter values with $\chi^2$/dof in the calculation are presented in Table 1. The two-component Erlang distribution with $m_2 = 2$ provides a good description on the data. As can be seen, the value of $T$ extracted from the $1^{st}$ leading jet spectra is significantly larger than that extracted from the $2^{nd}$ one. In the error range, $T$ extracted from the single-lepton channel jet spectra is approximately in agreement with that from the dilepton one.

The transverse momentum distributions for the subleading $b$-jets after the $Z + 2b$-jets selection corresponding to an integrated luminosity of 5.0 fb$^{-1}$, the soft-muon tagging (SMT) jets for opposite-sign and same-sign (OS-SS) events in $W$+1,2 jets samples in electron channels with an integrated luminosity of 4.6 fb$^{-1}$, and the light-quark jets produced in the same condition as that in Fig. 4(d) in $p$-$p$ collision at $\sqrt{s} = 7$ TeV are shown in Figs. 5(a)–5(c) respectively. The experimental data represented by the symbols were recorded by the CMS Collaboration [20] and the ATLAS Collaboration [19, 21]. The error bars indicate the total uncertainty. In Fig. 5(c), the error bars of the points in high-$p_T$ area present the marker size of the points from Ref. 19, in which the linear coordinate is used. The curves are our results calculated by the two-component Erlang distribution. The parameter values and the defined $T$ in the calculation are shown in Table 1 with values of $\chi^2$/dof. One can see that the experimental data are in good agreement with the two-component Erlang distribution with $m_2 = 2$. In the error range, the three effec-

tive temperatures extracted from the three distributions are approximately equal to each other.

Figure 6 shows some other jet $p_T$ distributions in $p$-$p$ collision at $\sqrt{s} = 7$ TeV. The symbols in (a)–(d) represent the experimental data which were recorded with the ATLAS detector corresponding to an integrated luminosity of 37 pb$^{-1}$ [22], the CMS detector corresponding to an integrated luminosity of 5.0 fb$^{-1}$ for the leading $b$-tagged jets in the $Z + 2b$-jets sample [20], the ATLAS detector corresponding to an integrated luminosity of 4.6 fb$^{-1}$ for the leading $b$-tagged jets in $e$+jets channels [23], and the ATLAS detector corresponding to an integrated luminosity of 4.6 fb$^{-1}$ for the leading $b$-tagged jets in $\mu$+jets channels [23], respectively. The statistical or systematic uncertainties are included in the error bars. For some data points with no error bars, we use the marker size as their errors in the calculation. The Monte Carlo results calculated by using the two-component Erlang distribution are indicated by the curves, and the corresponding parameters, defined $T$, and $\chi^2$/dof are listed in Table 1. The fitting distributions are in agreement with the experimental data. All the source numbers of the second components are 2. The values of $T$ extracted from the leading jets in Figs. 6(b)–6(d) are larger than that extracted from inclusive jets in Fig. 6(a). In addition, for the leading $b$-tagged jets, $T$ from $e$+jets channels is in agreement with that from $\mu$+jets channels within uncertainties.

The reconstructed jet $p_T$ spectra for the leading (squares), $2^{nd}$ (circles), $3^{rd}$ (triangles), $4^{th}$ (stars), and $5^{th}$ order jets (diamonds) in the electron ($e$+jets) channels produced in $p$-$p$ collision at $\sqrt{s} = 7$ TeV are indicated in Fig. 7. The symbols represent the experimental data collected by the ATLAS Collaboration corresponding to an integrated luminosity of 4.6 fb$^{-1}$ and a radius parameter of 0.4 within the pseudorapidity range $|\eta| < 2.5$ using anti-$k_T$ jet algorithm [12] for $p_T > 25$ GeV/$c$ jets [24]. In the figure, all the data have invisible error bars (statistical uncertainty only), so we measure the marker size as the errors used in the calculation. The curves are our fitted results with the two-component Erlang distribution, and the related parameter values with $\chi^2$ are given in Table 1. From the figure one can see that the fitted results are in agreement with the observed jet $p_T$ distributions. For different jet orders, we have $m_1 = 7$ and $m_2 = 2$. The value of $T$ decreases with increase of the jet order $O$. The figure display of the dependence of $T$ on $O$ will be discussed in the last part of this section.

In Figure 8, the leading jet $p_T$ distributions in (a) the 4-jet $t\bar{t}$ , (b) preselection, (c) $W$ boson+jets, and (d) 5-jet $t\bar{t}$ with an integrated luminosity of 4.7 fb$^{-1}$ in $p$-$p$ collision at $\sqrt{s} = 7$ TeV are shown. The symbols represent the experimental data recorded by the ATLAS Collaboration [25]. The error bars indicate the total uncertainty. The curves indicate the fitted results by the two-component Erlang distribution, and the corresponding values of free parameters, defined $T$, and $\chi^2$/dof are listed in Table 1. One can see that the two-component Erlang distribution with $m_2 = 2$ describes the data of the leading jet $p_T$ spectra, and the extracted effective temperature parameters have a smaller difference.

Figures 9(a) and 9(b) display $p_T$ distributions of the leading and fat jets in $p$-$p$ collision at $\sqrt{s} = 7$ TeV respectively, where the results are in the Lepton Plus Jets Channels using an integrated luminosity of 2.05 fb$^{-1}$. Figures 9(c)–9(f) give $p_T$ distributions of the leading jets in the same collision, and the corresponding integrated luminosity and lepton plus jets channels are shown in the panels. The symbols represent the experimental data of the ATLAS Collaboration [26–30]. The error bars indicate the experimental uncertainty.

Our calculated results by using the two-component Erlang distribution are presented by the curves in the figure. The values of free parameters, defined $T$, and $\chi^2$/dof are given in Table 1. One can see that the mentioned $p_T$ spectra for the leading and fat jets are fitted by the two-component Erlang distribution with $m_2 = 2$ and relatively larger $T$. In addition, in the error range, $T$ extracted from the jet spectra in $e$+jets channels is in agreement with that in $\mu$+jets channels.

The transverse momentum distributions of the leading jets produced in $p$-$p$ collision at $\sqrt{s} = 8$ TeV with an integrated luminosity of 14.3 fb$^{-1}$ in the $e$+jets and an integrated luminosity of 14.2 fb$^{-1}$ in the $\mu$+jets, after the resolved selection, are shown in Figs. 10(a) and 10(b) respectively. The experimental data (the squares) were recorded by the ATLAS Collaboration [31]. Meanwhile, the data (the squares) of the leading light jet $p_T$ distribution and the second leading light jet $p_T$ distribution from $p$-$p$ collision at $\sqrt{s} = 8$ TeV corresponding to a total integrated luminosity of 19.5 fb$^{-1}$ measured by the CMS Collaboration [32] are presented in Figs. 10(c) and 10(d) respectively. Moreover, the leading jet $p_T$ distribution and the subleading jet $p_T$ distribution in the dijet system using $p$-$p$ collision at $\sqrt{s} = 8$ TeV with an integrated luminosity of 20.3 fb$^{-1}$ are displayed in Figs. 10(e) and 10(f) respectively, where the squares represent the data of the ATLAS Collaboration [33]. In the figure, the error bars reflect the statistical uncertainty, and the curves are our results calculated by using the two-component Erlang distribution. The relevant parameter values with $\chi^2$/dof in our calculation are presented in Table 1. From the figure, one can see that the modelling results are in agreement with the data. Comparing with the leading jet spectra, the defined $T$ extracted from the subleading jet spectra exhibits a quickly decrease. The defined $T$ extracted from the light jet spectra shows relatively a little larger than that from the non-tagged jets spectra, or the two situations are approximately the same in the error range. Moreover, the defined $T$ corresponding to the leading jets from $e$+jets and $\mu$+jets channels in Figs. 10(a) and 10(b) are nearly the same.

The inclusive jet $p_T$ distributions and the large-$R$ jet $p_T$ distribution produced in $p$-$p$ collision at $\sqrt{s} = 8$ TeV are presented in Figure 11. The data (squares) in Fig. 11(a) were collected with the CMS detector corresponding to an integrated luminosity of 10.7 fb$^{-1}$ from a high-level trigger that accepted events containing at least one jet with $p_T > 320$ GeV/$c$ [34]. The data (squares) in Fig. 11(b) for $Z \to \mu\mu$ events were selected from the full 2012 run and amounted to a total integrated luminosity of 19.8 fb$^{-1}$ [35]. The data (squares) in Fig. 11(c) were collected by the ATLAS Collaboration corresponding to an integrated luminosity of 20 fb$^{-1}$ with an uncertainty of 2.8% [36]. In the figure, the curves indicate our fitted results. One can see that the modelling results are in good agreement with the experimental data. The related parameter values for Figs. 11(a) and 11(b) are given in Table 1, where the number of components is two and the source numbers of the second components are $m_2 = 2$. For Fig. 11(c), we have to use the three-component Erlang distribution with $m_1 = 29$, $p_{ti1} = (6.65\pm0.60)$ GeV/$c$, $k_1 = 0.396\pm0.036$, $m_2 = 14$, $p_{ti2} = (19.50 \pm 1.00)$ GeV/$c$, $k_2 = 0.204 \pm 0.036$, $m_3 = 2$, $p_{ti3} = (111.00 \pm 10.00)$ GeV/$c$, $T = 51.011 \pm 11.853$ GeV, and $\chi^2$/dof=0.377.

To see clearly the dependence of the effective temperature parameter $T$ on the centrality percentage $C$ in Pb-Pb collisions at $\sqrt{s_{NN}} = 2.76$ TeV, we present the relation $T - C$ in Fig. 12(a). The circles represent the effective temperature values obtained from Figure

3 and listed in Table 1, and the curve is our fitted result by an exponential function of

$$T = (-0.125 \pm 0.020) \exp\left[ - \frac{C}{(10.500 \pm 3.000)} \right] + (5.878 \pm 0.010) \tag{7}$$

with $\chi^2$/dof=0.0002, where $T$ is in the units of GeV and $C$ is in %. One can see that $T$ slightly increases with increase of $C$, and a saturation effect quickly appears in semi-central collisions, or $T$ has no obvious change in the error range with increase of $C$. In addition, to see clearly the dependence of the effective temperature parameter $T$ on the jet order $O$ in $p$-$p$ collision at $\sqrt{s} = 7$ TeV, we present the relation $T - O$ in Fig. 12(b). The circles represent the effective temperature values obtained from Figure 7 and listed in Table 1, and the curve is our fitted result by an exponential function of

$$T = (54.30 \pm 3.00) \exp\left[ - \frac{O}{(1.43 \pm 0.10)} \right] + (4.55 \pm 1.00) \tag{8}$$

with $\chi^2$=0.129, where $T$ is in the units of GeV. One can see that $T$ decreases with increase of $O$.

The dependences of the effective temperature parameter $T$ on other factors such as $l$ and di-$l$ channels (a), $\mu(\mu\mu)$ and $e(ee)$ channels (b), leading and sub-leading jets (c), as well as size of interacting system (d) are displayed in Figure 13, where the symbols represent the effective temperature values obtained from the above figures and listed in Table 1. One can see that a high center-of-mass energy results in a high effective temperature, different lepton channels show approximately the same effective temperature in the error range, and the leading jets correspond to a high effective temperature comparing with the sub-leading jets. At the same time, $T$ slightly decreases with increase of the size of interacting system, or $T$ is approximately not related to the size in the error range. The former case can be explained by the influence of jet quenching effect (quickly energy loss) which exists in Au-Au collisions and doesn't exist in $p$-$p$ collision.

# 4 Conclusions

From the above discussions, we obtain following conclusions.

(a) The transverse momentum distributions, of various jets produced in $p$-$p$, $p$-$\bar{p}$, $d$-Au, Au-Au, and Pb-Pb collisions over an energy range from 0.2 to 8 TeV in different additional selection conditions, are described by using the multi-component Erlang distribution in the framework of the multi-source thermal model which reflects the reaction types in interacting system and multiple temperatures emission. The calculated results are in good agreement with the experimental data measured by the STAR, D0, CDF II, ALICE, ATLAS, and CMS Collaborations.

(b) Except for one group data in Fig. 11(c) which is described by the three-component Erlang distribution, the data of $p_T$ spectra for mentioned jets are fitted by the two-component Erlang distribution. The source numbers of the first components are greater than or equal to 2, while the source numbers of the second components are mostly 2. In $p_T$ distribution, the first-component in charge of low-$p_T$ jets indicates strong scattering interactions between two quarks or among more quarks and gluons and accounted for a

larger proportion, and the second-component for high-$p_T$ region means harder head-on scattering between two quarks.

(c) The effective temperature parameter $T$ is higher, which means that the transverse excitation of emission source is very violent. From our study, $T$ depends on the center-of-mass energy, system size, centrality interval, jet type, jet order, channel of detection system, and origination. Generally, $T$ increases with increase of center-of-mass energy, that renders the larger the center-of-mass energy is, the more violent transverse excitation of the interacting system is. Besides, at the same center-of-mass energy, there is a slightly negative correlation between $T$ and the system size, or $T$ is approximately independent of the size in the error range. The former case reflects that, in relatively complex collision system, there is a jet quenching effect (quickly energy loss) in the case of high energy quark and gluon jets penetrating through the dense deconfined matter.

(d) From $p_T$ distributions of charged jets produced in Pb-Pb collisions at $\sqrt{s_{NN}} = 2.76$ TeV with different centrality intervals analyzed by using the two-component Erlang distribution, we know that $T$ slightly increases with increase of the centrality percentage $C$ and quickly saturates in semi-central collisions, or $T$ has no obvious change in the error range with increase of $C$. In addition, as expected, the extracted effective temperature from the reconstructed jets $p_T$ spectra produced in electron channels in $p$-$p$ collisions at $\sqrt{s} = 7$ TeV decreases with increase of the jet order from the $1^{st}$ to $5^{th}$.

(e) At the same energy, the effective temperature extracted from the leading jets is much higher than that from the subleading jets. This is a natural result because the leading jets are produced through more violent scattering. The effective temperature extracted from tagged jets (such as light-quark jets and $b$-quark jets) seems to be higher than that from non-tagged jets, which reveals that the hadron jets originated from quark jets carry more energy and the leading jets primarily originate from quark jets. The effective temperatures extracted from different lepton and dilepton channel jets are approximately the same in the error range, which reflects the common property in these jets.

**Conflict of Interests**

The authors declare that there is no conflict of interests regarding the publication of this paper.

**Acknowledgments**

One of the authors (Fu-Hu Liu) thanks Prof. Dr. Charles Gale, Prof. Dr. Sangyong Jeon, and the members of the Physics Department of McGill University, Canada, for their hospitality, where this work was partly finished. The authors' work was supported by the National Natural Science Foundation of China under Grant No. 10975095, the Open Research Subject of the Chinese Academy of Sciences Large-Scale Scientific Facility under Grant No. 2060205, the Shanxi Provincial Natural Science Foundation under Grant No. 2013021006, and the Foundation of Shanxi Scholarship Council of China under Grant No. 2012-012.

# References


[1] D. H. Rischke, Prog. Part. Nucl. Phys. **52**, 197–296 (2004).

[2] D. H. Rischke, Nucl. Phys. A **698**, 153–163 (2002).

[3] D. d'Enterria, arXiv:0902.2011v2.

[4] BRAHMS Collaboration (I. Arsene *et al.*), Nucl. Phys. A **757**, 1–27 (2005).

[5] S. Domdey, B. Z. Kopeliovich, H. J. Pirner, Nucl. Phys. A **856**, 134–153 (2011).

[6] N. Gupta, A Study of Fluctuations in Multiplicity Distributions at Ultra-Relativistic Heavy Ion Interactions, submitted (University of Jammu 2008).

[7] L. V. Hove, Phys. Lett. B **118**, 138–140 (1982).

[8] H.-R. Wei, Y.-H. Chen, L.-N. Gao, F.-H. Liu, Advances in High Energy Physics **2014**, 782631 (2014).

[9] STAR Collaboration (L. Adamczyk *et al.*), Phys. Rev. Lett. **112**, 122301 (2014).

[10] Jan Kapitan for the STAR Collaboration, J. Phys. Conf. Ser. **270**, 012015 (2011).

[11] STAR Collaboration (L. Adamczyk *et al.*), arXiv:1205.2735v1.

[12] M. Cacciari, G. P. Salam, G. Soyez, JHEP **04**, 063 (2008).

[13] D0 Collaboration (V. M. Abazov *et al.*), Phys. Rev. D **87**, 092010 (2013).

[14] D0 Collaboration (V. M. Abazov *et al.*), Phys. Rev. D **88**, 092001 (2013).

[15] CDF II Collaboration, CDF note CDF-PUB-JET-PUBLIC-10199.

[16] ALICE Collaboration (B. Abelev *et al.*), JHEP **04**, 013 (2014).

[17] CMS Collaboration (S. Chatrchyan *et al.*), Eur. Phys. J. C, **74**, 3014 (2014).

[18] ATLAS Collaboration (G. Aad *et al.*), JHEP **05**, 128 (2012).

[19] ATLAS Collaboration (G. Aad *et al.*), Eur. Phys. J. C **73**, 2676 (2013).

[20] CMS Collaboration (S. Chatrchyan *et al.*), JHEP **06**, 120 (2014).

[21] ATLAS Collaboration (G. Aad *et al.*), JHEP **05**, 068 (2014).

[22] ATLAS Collaboration (G. Aad *et al.*), Nucl. Phys. B **875**, 483-535 (2013).

[23] ATLAS Collaboration (G. Aad *et al.*), Phys. Rev D **90**, 072004 (2014).

[24] ATLAS Collaboration (G. Aad *et al.*), JHEP **01**, 020 (2015).

[25] ATLAS Collaboration (G. Aad *et al.*), Phys. Rev D **86**, 091103 (2012).

[26] ATLAS Collaboration (G. Aad *et al.*), Eur. Phys. J. C **72**, 2083 (2012).

[27] ATLAS Collaboration (G. Aad *et al.*), JHEP **09**, 041 (2012).

[28] ATLAS Collaboration (G. Aad *et al.*), Phys. Rev D **88**, 012004 (2013).

[29] ATLAS Collaboration, ATLAS NOTE ATLAS-CONF-2011-087.

[30] ATLAS Collaboration, ATLAS NOTE ATLAS-CONF-2011-070.

[31] ATLAS Collaboration, ATLAS NOTE ATLAS-CONF-2013-052, EPJ Web of Conferences **60**, 20044 (2013).

[32] CMS Collaboration, CMS PAS B2G-12-008.

[33] ATLAS Collaboration (G. Aad *et al.*), JHEP **04**, 031 (2014).

[34] CMS Collaboration (V. Khachatryan *et al.*), Phys. Rev. D **90**, 032005 (2014).

[35] CMS Collaboration, CMS PAS JME-13-005.

[36] ATLAS Collaboration (G. Aad *et al.*), JHEP **11**, 118 (2014).

[37] F.-H. Liu, Phys. Rev. C **69**, 057601 (2004).

[38] F.-H. Liu, Phys. Rev. C **78**, 014902 (2008).

[39] F.-H. Liu, Nucl. Phys. A **810**, 159–172 (2008).

Table 1. Values of free parameters, defined $T$, and $\chi^2$/dof ($\chi^2$) corresponding to the curves in the figures, where $\chi^2$ is given in bracket if the number of data points is less than 6 which is the number of free parameters and normalization constant. The errors of $m_j$ are estimated to be 0.

| Figure, type | $m_1$ | $p_{ti1}$ (GeV/$c$) | $k_1$ | $m_2$ | $p_{ti2}$ (GeV/$c$) | $T$ (GeV) | $\chi^2$/dof ($\chi^2$) |
|---|---|---|---|---|---|---|---|
| 1(a) | 2 | $1.70 \pm 0.20$ | $0.860 \pm 0.030$ | 2 | $3.25 \pm 0.10$ | $1.917 \pm 0.205$ | 0.328 |
| 1(b) | 2 | $1.60 \pm 0.20$ | $0.900 \pm 0.030$ | 2 | $3.55 \pm 0.20$ | $1.795 \pm 0.215$ | 0.189 |
| 1(c) | 2 | $1.82 \pm 0.07$ | $0.994 \pm 0.002$ | 2 | $5.00 \pm 0.50$ | $1.839 \pm 0.070$ | 0.038 |
| 1(d) | 11 | $1.25 \pm 0.05$ | $0.890 \pm 0.020$ | 8 | $2.47 \pm 0.05$ | $1.384 \pm 0.071$ | (0.084) |
| 2(a) | 2 | $8.80 \pm 0.80$ | $0.830 \pm 0.030$ | 2 | $22.80 \pm 1.50$ | $11.180 \pm 1.022$ | 0.132 |
| 2(b) | 2 | $8.80 \pm 0.70$ | $0.840 \pm 0.030$ | 2 | $23.00 \pm 1.50$ | $11.072 \pm 0.974$ | 0.191 |
| 2(c) | 2 | $10.20 \pm 1.00$ | $0.900 \pm 0.030$ | 2 | $26.60 \pm 2.00$ | $11.840 \pm 1.257$ | 0.393 |
| 2(d) | 2 | $12.00 \pm 8.00$ | $0.996 \pm 0.001$ | 2 | $34.00 \pm 0.50$ | $12.088 \pm 7.968$ | 0.186 |
| 3(a) | 2 | $5.20 \pm 0.04$ | $0.900 \pm 0.020$ | 2 | $11.20 \pm 0.40$ | $5.800 \pm 0.253$ | 0.044 |
| 3(b) | 2 | $5.50 \pm 0.03$ | $0.950 \pm 0.010$ | 2 | $12.70 \pm 0.40$ | $5.860 \pm 0.143$ | 0.097 |
| 3(c) | 2 | $5.50 \pm 0.02$ | $0.950 \pm 0.010$ | 2 | $12.80 \pm 0.50$ | $5.865 \pm 0.143$ | 0.011 |
| 3(d) | 2 | $5.60 \pm 0.03$ | $0.960 \pm 0.010$ | 2 | $12.70 \pm 0.80$ | $5.884 \pm 0.145$ | 0.054 |
| 4(a), $1^{st}$ | 2 | $13.00 \pm 2.00$ | $0.620 \pm 0.080$ | 2 | $40.00 \pm 5.00$ | $23.260 \pm 4.058$ | 0.100 |
| 4(a), $2^{nd}$ | 2 | $11.50 \pm 1.00$ | $0.850 \pm 0.050$ | 2 | $28.00 \pm 5.00$ | $13.975 \pm 1.891$ | 0.185 |
| 4(b), lepton | 2 | $28.00 \pm 2.00$ | $0.907 \pm 0.010$ | 2 | $100.00 \pm 30.00$ | $30.160 \pm 2.377$ | 0.019 |
| 4(b), dilepton | 2 | $25.00 \pm 2.00$ | $0.850 \pm 0.050$ | 2 | $47.00 \pm 5.00$ | $28.300 \pm 3.246$ | 0.055 |
| 4(c), inclusive | 2 | $42.00 \pm 2.00$ | $0.998 \pm 0.001$ | 2 | $115.00 \pm 10.00$ | $42.164 \pm 2.000$ | 0.619 |
| 4(c), split | 2 | $34.00 \pm 3.00$ | $0.994 \pm 0.003$ | 2 | $87.00 \pm 10.00$ | $34.318 \pm 2.996$ | 3.769 |
| 4(d), lepton | 2 | $21.90 \pm 2.00$ | $0.890 \pm 0.090$ | 2 | $40.50 \pm 10.00$ | $23.946 \pm 4.642$ | 0.095 |
| 4(d), dilepton | 2 | $22.50 \pm 2.00$ | $0.880 \pm 0.100$ | 2 | $47.00 \pm 10.00$ | $25.440 \pm 5.629$ | 0.392 |
| 5(a) | 2 | $13.50 \pm 1.00$ | $0.910 \pm 0.050$ | 2 | $50.00 \pm 20.00$ | $16.785 \pm 3.282$ | 0.303 |
| 5(b) | 2 | $11.20 \pm 1.00$ | $0.820 \pm 0.100$ | 2 | $28.00 \pm 10.00$ | $14.224 \pm 3.606$ | 0.312 |
| 5(c) | 2 | $18.00 \pm 2.00$ | $0.810 \pm 0.100$ | 2 | $29.00 \pm 5.00$ | $20.090 \pm 3.896$ | 0.067 |
| 6(a) | 4 | $12.70 \pm 0.90$ | $0.900 \pm 0.020$ | 2 | $44.00 \pm 4.00$ | $15.830 \pm 1.286$ | 0.187 |
| 6(b) | 6 | $11.50 \pm 1.00$ | $0.710 \pm 0.100$ | 2 | $80.00 \pm 30.00$ | $31.365 \pm 11.896$ | 0.661 |
| 6(c) | 4 | $18.80 \pm 1.00$ | $0.960 \pm 0.010$ | 2 | $92.00 \pm 10.00$ | $21.728 \pm 1.401$ | 0.181 |
| 6(d) | 5 | $15.20 \pm 0.80$ | $0.770 \pm 0.080$ | 2 | $42.00 \pm 5.00$ | $21.364 \pm 3.804$ | 0.173 |
| 7, leading | 7 | $14.00 \pm 1.00$ | $0.610 \pm 0.050$ | 2 | $58.00 \pm 2.00$ | $31.160 \pm 3.143$ | (0.069) |
| 7, $2^{nd}$ | 7 | $9.60 \pm 0.08$ | $0.740 \pm 0.050$ | 2 | $42.00 \pm 2.00$ | $18.024 \pm 2.217$ | (0.367) |
| 7, $3^{rd}$ | 7 | $6.10 \pm 0.50$ | $0.620 \pm 0.050$ | 2 | $23.00 \pm 1.00$ | $12.522 \pm 1.287$ | (0.434) |
| 7, $4^{th}$ | 7 | $4.70 \pm 1.00$ | $0.780 \pm 0.050$ | 2 | $18.80 \pm 1.50$ | $7.802 \pm 1.287$ | (0.281) |
| 7, $5^{th}$ | 7 | $4.00 \pm 0.70$ | $0.820 \pm 0.040$ | 2 | $15.00 \pm 1.50$ | $5.980 \pm 0.888$ | (0.128) |
| 8(a) | 5 | $22.00 \pm 2.00$ | $0.820 \pm 0.030$ | 2 | $82.00 \pm 4.00$ | $32.800 \pm 3.114$ | 0.177 |
| 8(b) | 6 | $17.60 \pm 1.00$ | $0.880 \pm 0.030$ | 2 | $79.00 \pm 5.00$ | $24.968 \pm 2.651$ | 0.619 |
| 8(c) | 5 | $23.00 \pm 3.00$ | $0.580 \pm 0.050$ | 2 | $81.00 \pm 5.00$ | $47.360 \pm 5.016$ | 0.408 |
| 8(d) | 6 | $18.00 \pm 1.00$ | $0.820 \pm 0.040$ | 2 | $100.00 \pm 10.00$ | $32.760 \pm 4.520$ | 0.799 |
| 9(a) | 4 | $24.90 \pm 2.00$ | $0.880 \pm 0.040$ | 2 | $89.00 \pm 7.00$ | $32.592 \pm 4.180$ | 1.022 |
| 9(b) | 6 | $36.50 \pm 1.00$ | $0.850 \pm 0.030$ | 2 | $132.00 \pm 8.00$ | $50.825 \pm 4.364$ | 0.112 |
| 9(c) | 6 | $18.50 \pm 1.00$ | $0.880 \pm 0.050$ | 2 | $120.00 \pm 50.00$ | $30.680 \pm 8.581$ | 0.427 |
| 9(d) | 6 | $19.10 \pm 1.00$ | $0.930 \pm 0.030$ | 2 | $160.00 \pm 50.00$ | $28.963 \pm 6.040$ | 0.453 |
| 9(e) | 7 | $16.00 \pm 1.00$ | $0.870 \pm 0.050$ | 2 | $109.00 \pm 15.00$ | $28.090 \pm 5.908$ | 0.815 |
| 9(f) | 9 | $11.60 \pm 1.00$ | $0.750 \pm 0.050$ | 2 | $180.00 \pm 100.00$ | $53.700 \pm 26.588$ | 0.731 |
| 10(a) | 9 | $11.00 \pm 0.70$ | $0.700 \pm 0.070$ | 4 | $41.00 \pm 3.00$ | $20.000 \pm 3.143$ | 0.196 |
| 10(b) | 9 | $10.90 \pm 0.70$ | $0.710 \pm 0.050$ | 4 | $40.00 \pm 2.00$ | $19.339 \pm 2.209$ | 0.138 |
| 10(c) | 5 | $15.20 \pm 2.00$ | $0.540 \pm 0.100$ | 2 | $69.00 \pm 10.00$ | $39.948 \pm 8.500$ | 0.137 |
| 10(d) | 5 | $5.80 \pm 1.00$ | $0.580 \pm 0.100$ | 2 | $26.00 \pm 5.00$ | $14.284 \pm 3.441$ | 0.298 |
| 10(e) | 2 | $25.30 \pm 2.00$ | $0.830 \pm 0.030$ | 2 | $61.00 \pm 3.00$ | $31.369 \pm 2.634$ | 0.053 |
| 10(f) | 2 | $12.50 \pm 0.50$ | $0.970 \pm 0.003$ | 2 | $47.00 \pm 2.00$ | $12.877 \pm 0.507$ | 0.295 |
| 11(a) | 4 | $45.80 \pm 4.00$ | $0.969 \pm 0.010$ | 2 | $118.00 \pm 5.00$ | $48.038 \pm 4.080$ | 0.392 |
| 11(b) | 6 | $3.00 \pm 0.10$ | $0.760 \pm 0.020$ | 2 | $19.00 \pm 1.00$ | $6.840 \pm 0.460$ | 0.062 |

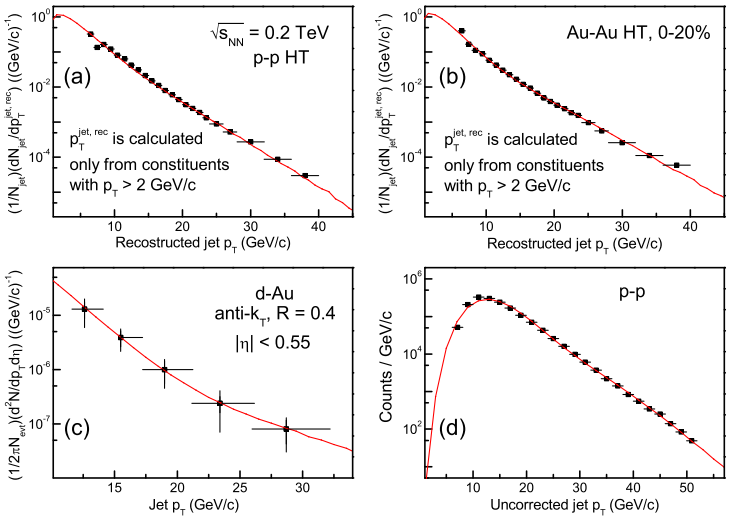


Fig. 1. Transverse momentum spectra of HT trigger jets in $p$-$p$ collision (a), HT trigger jets in 0–20% central Au-Au collisions (b), jets from $d$-Au collisions (c), and uncorrected jets in $p$-$p$ collision (d) at $\sqrt{s_{NN}} = 0.2$ TeV. The symbols represent the experimental data of the STAR Collaboration [9–11] and the curves are our results calculated by using the two-component Erlang distribution in the framework of the multi-source thermal model. All the calculations are performed by the Monte Carlo method.

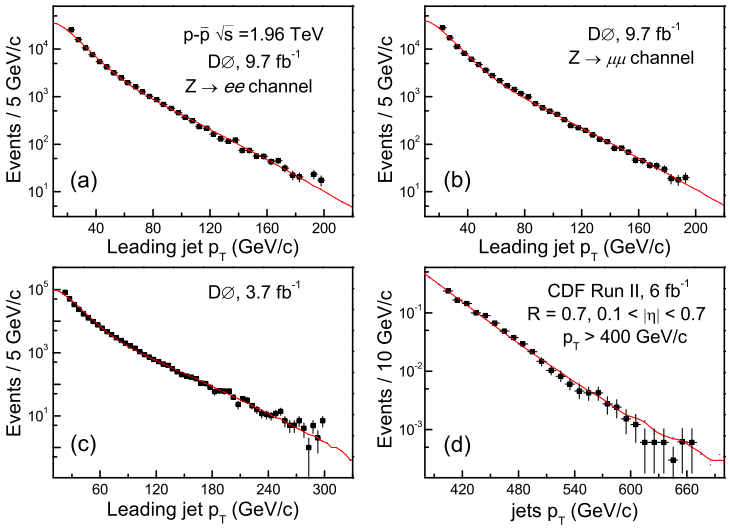


Fig. 2. Transverse momentum spectra for the leading jets (a)–(c) and all the jet candidates (d) produced in $p$-$\bar{p}$ collision at $\sqrt{s} = 1.96$ TeV. The symbols in Figs. 2(a)/2(b) and Figs. 2(c)/2(d) represent the experimental data of the D0 Collaboration [13, 14] and the CDF II Collaboration [15] respectively. The curves are our results calculated by using the two-component Erlang distribution.

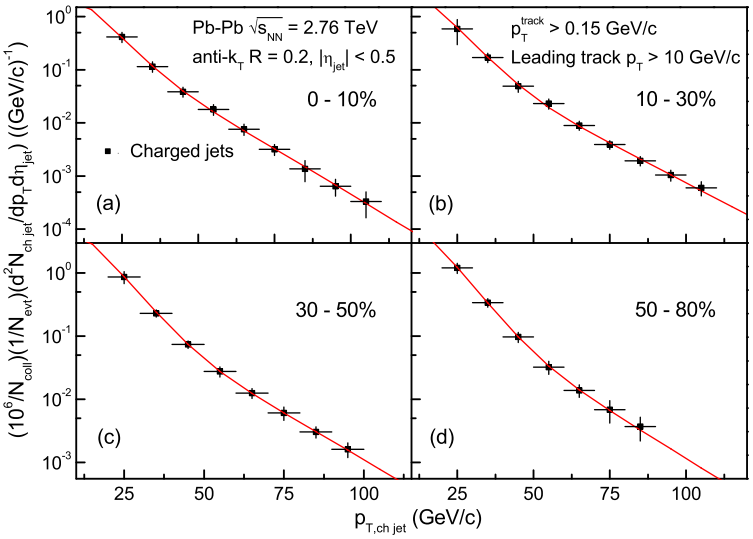


Fig. 3. Charged jet $p_T$ spectra produced in Pb-Pb collisions at $\sqrt{s_{NN}} = 2.76$ TeV in different centrality intervals of 0–10% (a), 10–30% (b), 30–50% (c), and 50–80% (d). The symbols represent the experimental data of the ALICE Collaboration [16] and the curves are our results calculated by using the two-component Erlang distribution.

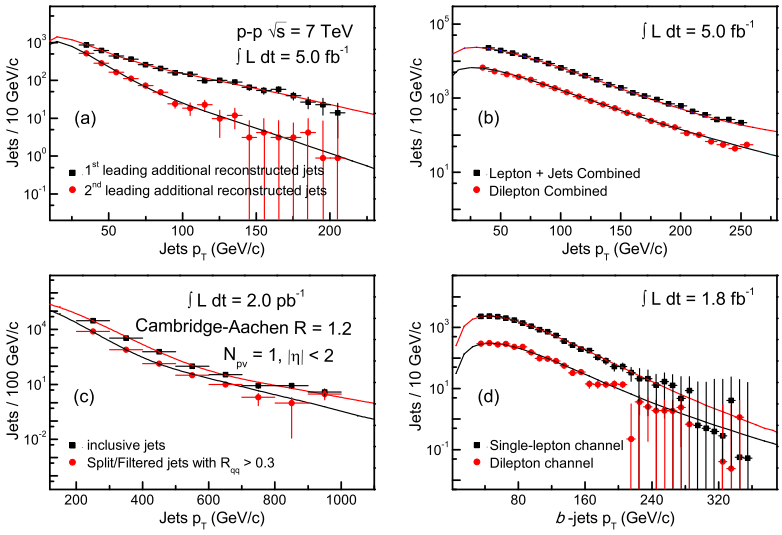


Fig. 4. Jet $p_T$ spectra produced in $p$-$p$ collision at $\sqrt{s} = 7$ TeV for different situations shown in the panels and text. The symbols shown in Figs. 4(a)/4(b) and Figs. 4(c)/4(d) represent the experimental data of the CMS Collaboration [17] and the ATLAS Collaboration [18, 19] respectively. The curves are our modelling results.

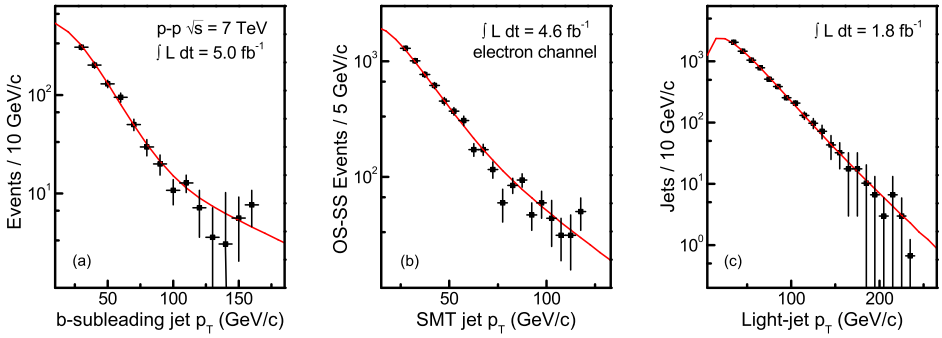


Fig. 5. Transverse momentum spectra for the subleading $b$-jets (a), the SMT jets (b), and the light-quark jets (c) produced in $p$-$p$ collision at $\sqrt{s} = 7$ TeV. The symbols represent the experimental data of the CMS Collaboration [20] and the ATLAS Collaboration [19, 21]. The curves are our modelling results.

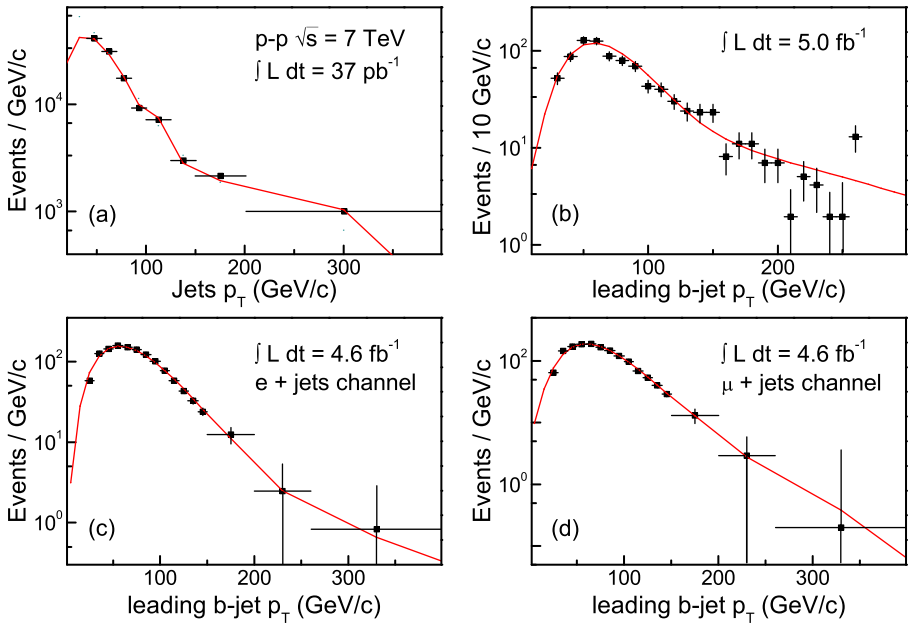


Fig. 6. Some other jet $p_T$ spectra in $p$-$p$ collision at $\sqrt{s} = 7$ TeV for different situations shown in the panels and text. The symbols shown in Figs. 6(a), 6(b), and 6(c)/6(d) represent the experimental data of the ATLAS [22], CMS [20], and ATLAS Collaborations [23], respectively. The curves are our modelling results.

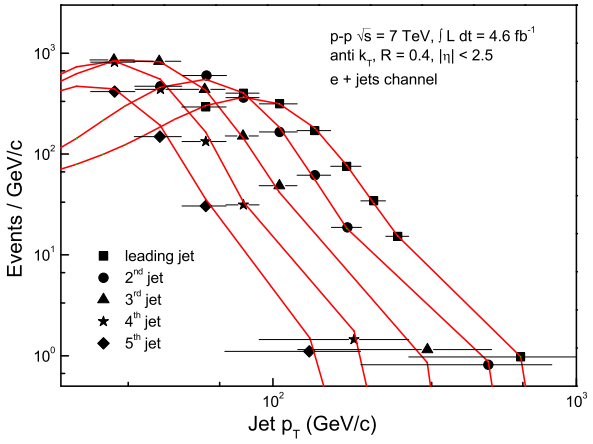


Fig. 7. The transverse momentum spectra for the leading, $2^{nd}$ , $3^{rd}$, $4^{th}$, and $5^{th}$ order jets in the electron ($e$+jets) channels produced in $p$-$p$ collision at $\sqrt{s} = 7$ TeV. The symbols represent the experimental data of the ATLAS Collaboration [24] and the curves are our modelling results.

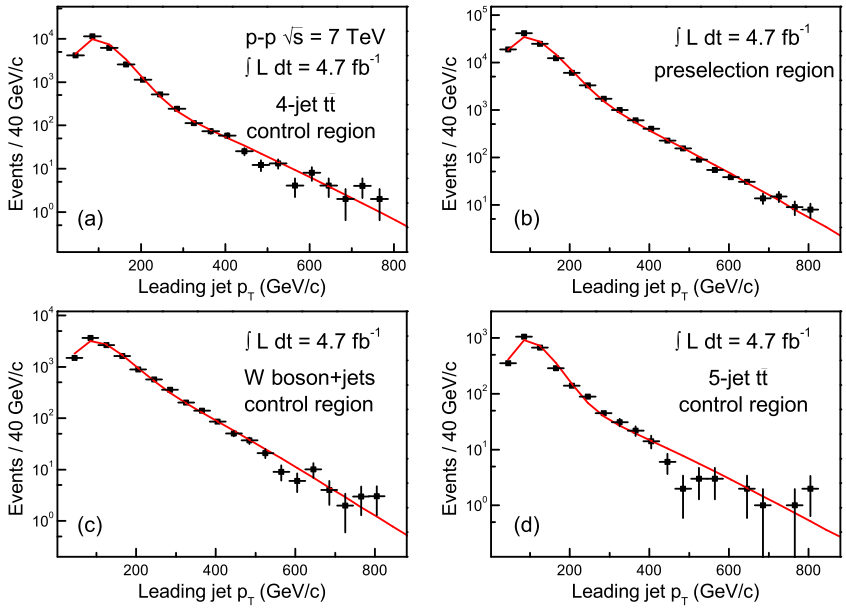


Fig. 8. The leading jet $p_T$ distributions in (a) the 4-jet $t\bar{t}$, (b) preselection, (c) $W$ boson+jets, and (d) 5-jet $t\bar{t}$ with an integrated luminosity of 4.7 fb$^{-1}$ in $p$-$p$ collision at $\sqrt{s} = 7$ TeV. The symbols represent the experimental data of the ATLAS Collaboration [25] and the curves are our modelling results.

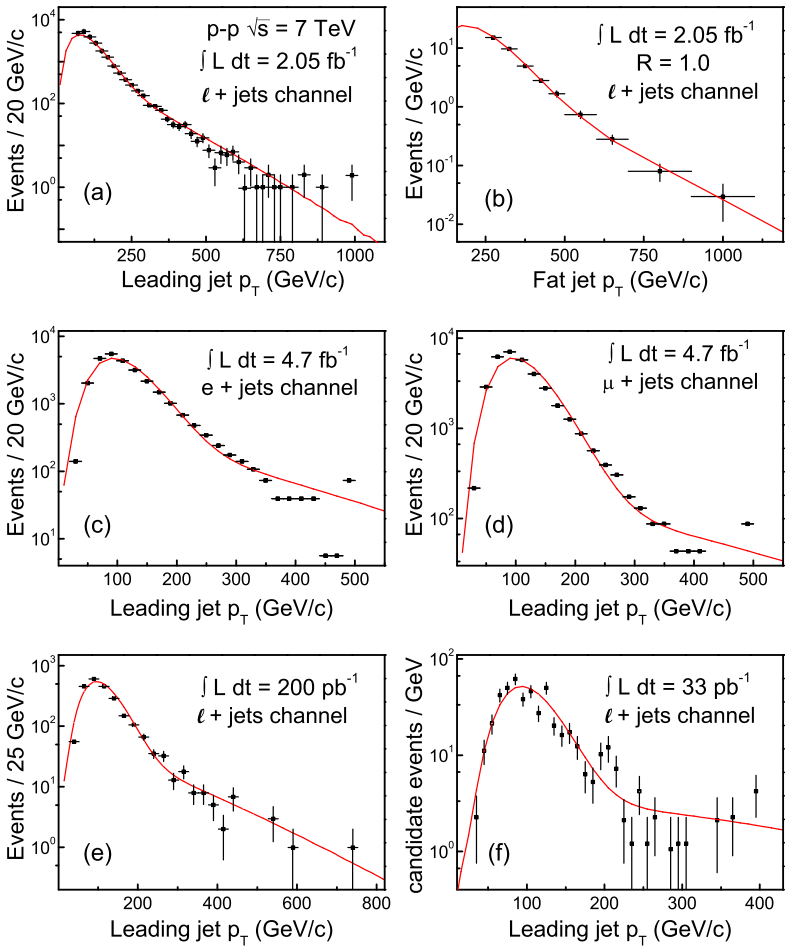


Fig. 9. Transverse momentum distributions of the leading and fat jets produced in $p$-$p$ collision at $\sqrt{s} = 7$ TeV with different channels and integrated luminosities shown in the panels and text. The symbols represent the experimental data of the ATLAS Collaboration [26–30] and the curves are our modelling results.

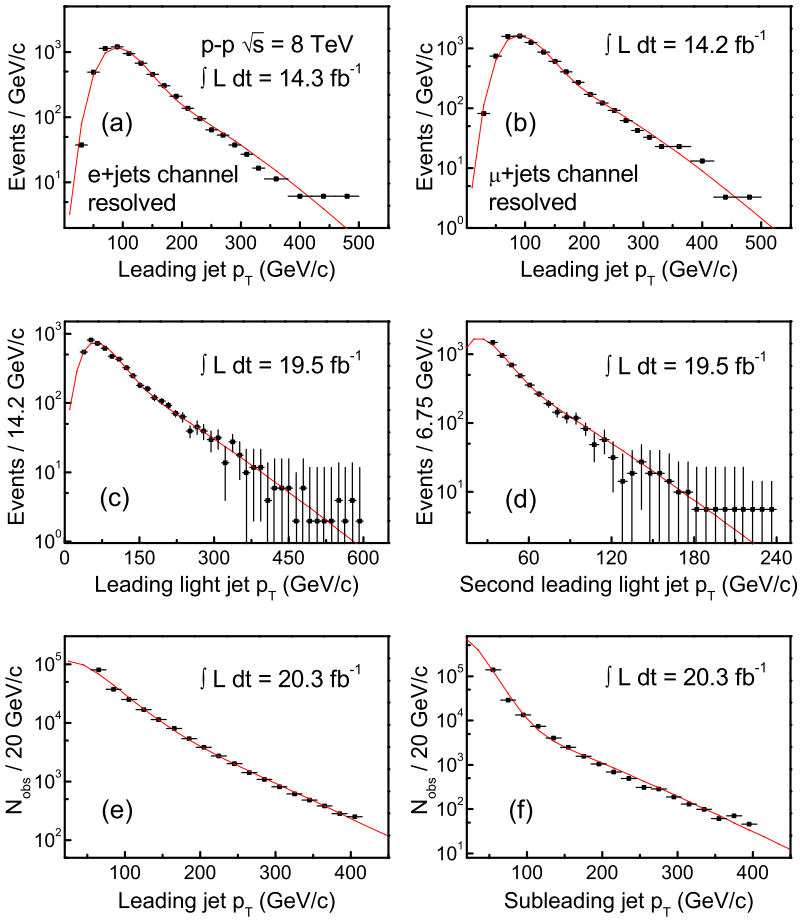


Fig. 10. Transverse momentum distributions of different types of jets produced in $p$-$p$ collision at $\sqrt{s} = 8$ TeV with different selected conditions shown in the panels and text. The symbols shown in Figs. 10(a)/10(b), 10(c)/10(d), and 10(e)/10(f) represent the experimental data of the ATLAS [31], CMS [32], and ATLAS Collaborations [33], respectively. The curves are our modelling results.

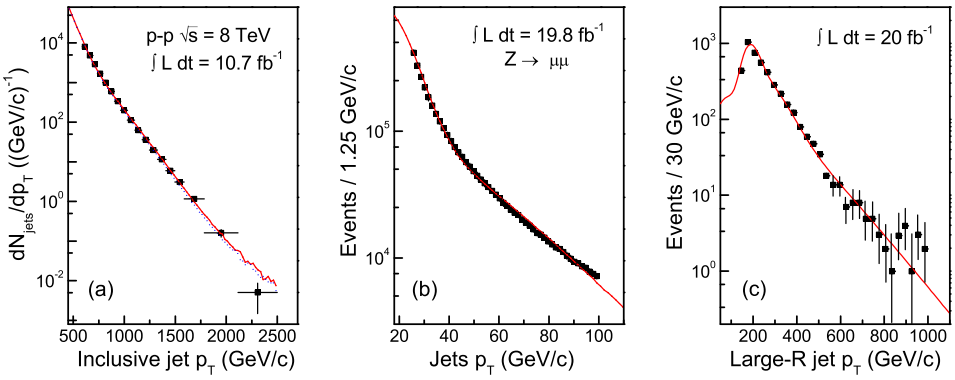


Fig. 11. (a) and (b) Inclusive jet $p_T$ spectra and (c) the large-$R$ jet $p_T$ spectrum produced in $p$-$p$ collision at $\sqrt{s} = 8$ TeV. The symbols shown in Figs. 11(a)/11(b) and 11(c) represent the experimental data of the CMS [34, 35] and ATLAS Collaborations [36], respectively. The curves are our modelling results, where the two-component Erlang distribution is used for Figs. 11(a) and 11(b), and the three-component Erlang distribution is used for Fig. 11(c).

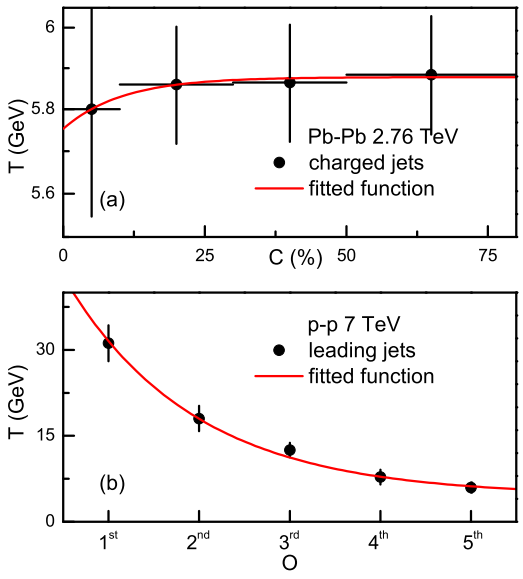


Fig. 12. Dependences of defined effective temperature parameter $T$ on centrality percentage $C$ in Pb-Pb collisions at $\sqrt{s_{NN}} = 2.76$ TeV (a) and on jet order $O$ in $p$-$p$ collision at $\sqrt{s} = 7$ TeV (b). The symbols represent $T$ values obtained from Figs. 3 and 7 (listed in Table 1) respectively, and the curves are our fitted results which are presented in Eqs. (7) and (8) respectively.

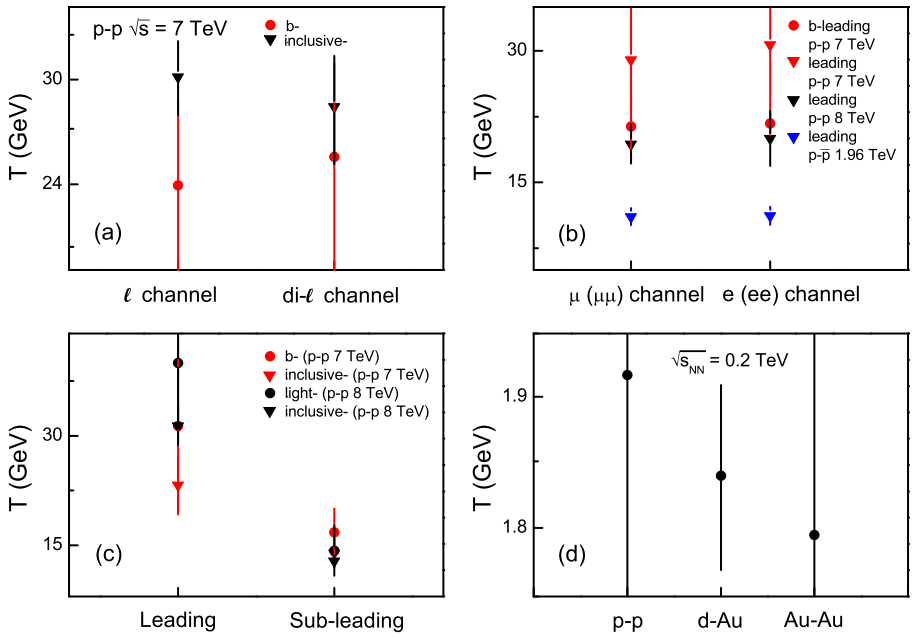


Fig. 13. Dependences of $T$ on $l$ and di-$l$ channels (a), $\mu(\mu\mu)$ and $e(ee)$ channels (b), leading and sub-leading jets (c), as well as size of interacting system (d). The symbols represent $T$ values obtained from related figures and listed in Table 1.